Grazing-incidence small-angle X-ray scattering from Ge nanodots self-organized on Si(001) examined with soft X-rays

Takayoshi Yamamoto,[a] Hiroshi Okuda,[b]* Kohki Takeshita,[a] Noritaka Usami,[c] Yoshinori Kitajima[d] and Hiroki Ogawa[e]

[a]Graduate School of Engineering, Kyoto University, Yoshida Honmachi, Kyoto 606-8501, Japan, [b]Department of Materials Science and Engineering, Kyoto University, Yoshida Honmachi, Sakyo-ku, Kyoto 606-8501, Japan, [c]Institute for Materials Research, Tohoku University, 2-1-1 Katahira, Sendai 980-8577, Japan, [d]Photon Factory, High Energy Accelerator Research Organization, Oho, Tsukuba 305-0801, Japan, and [e]JASRI, SPring-8, Kohto, Sayo 679-5198, Japan.
*E-mail: okuda.hiroshi.5a@kyoto-u.ac.jp

Grazing-incidence small-angle X-ray scattering (GISAXS) measurements with soft X-rays have been applied to Ge nanodots capped with a Si layer. Spatially anisotropic distribution of nanodots resulted in strongly asymmetric GISAXS patterns in the q_y direction in the soft X-ray region, which have not been observed with conventional hard X-rays. However, such apparent differences were explained by performing a GISAXS intensity calculation on the Ewald sphere, *i.e.* taking the curvature of Ewald sphere into account.

1. Introduction

Grazing-incidence small-angle X-ray scattering (GISAXS) measurements, mostly made with hard X-rays (HX), have been used to examine the nanostructure of materials (Renaud *et al.*, 2009) such as metallic nanoparticles (Levine *et al.*, 1989), self-organized polymer films (Lee *et al.*, 2005; Busch *et al.*, 2007; Müller-Buschbaum, 2013) and semiconducting or metallic materials (Li *et al.*, 2002; Rauscher *et al.*, 1999; Metzger *et al.*, 1999; Schmidbauer *et al.*, 1999). *In situ* two-dimensional GISAXS measurement is a powerful tool for examining the kinetics of self-organization or phase transformation occurring in thin films (Gibaud *et al.*, 2003). Extension of GISAXS measurements into the soft X-ray (SX) region (*e.g.* Okuda *et al.*, 2009, 2011) is a profitable approach because better depth resolution and use of anomalous dispersion of light elements such as Si and P, *i.e.* element-sensitive analysis for light elements, are expected. However, this approach is not yet popular due to some technical difficulties in measurements and analysis. For GISAXS measurements in the SX region, the equipment and sample should be placed in a vacuum, and the large curvature of the Ewald sphere may give an apparent distortion of the GISAXS pattern when measurements are made with a fixed angle of incidence and using two-dimensional detectors such as image plates or charge coupled devices, whose use is necessary for *in situ* measurements.

From our previous work on GISAXS analysis with hard X-rays, the shape of the Si-capped Ge nanodots used in the present work was isotropic in the in-plane direction (Okuda *et al.*, 2002, 2010), showing the same gyration radius in the in-plane direction and without any streaks originating from facets. This is reasonable since the surface diffusion during the initial stage of growing the cap layer is known to induce alloying with the nanodot layer even at very low growth temperatures, which often results in loss of facet structure and relating shape change of nanodots (Kubler *et al.*, 1998; Petz & Floro, 2011). When GISAXS measurements were made with both soft and hard X-rays for Ge nanodots self-organized by molecular beam epitaxy (MBE), the patterns were similar and the difference in the GISAXS patterns was explained by the refractive indices and also by a small effect of the curvature of the Ewald sphere, from simulations using the distorted wave Born approximation (DWBA) (Okuda *et al.*, 2009). In the present work, GISAXS patterns for small Ge nanodots grown by gas-source MBE capped with Si have been examined with soft and hard X-rays and a model calculated based on the DWBA.

2. Experimental

The samples used in the present measurements were grown by gas-source MBE on a Si (001) substrate for a single layer of nanodots and capped with a Si layer (Okuda *et al.*, 2010). The thickness of the cap layer determined by reflectivity was 40.1 nm. GISAXS measurements were conducted with photon energies of 1.77 keV at BL11B of the Photon Factory (Okuda *et al.*, 2009) and 12.4 keV at BL03XU of SPring-8 (Ogawa *et*

al., 2013). Image plates were used in both measurements. The change in the GISAXS patterns with in-plane rotation was recorded every 22.5° for 1.77 keV energy and every 2° for 12.4 keV.

3. Results and discussions

The GISAXS patterns obtained at 1.77 keV (SX) and 12.4 keV (HX) are shown in Fig. 1. They show two common characteristics. One is a strong streak extending in the q_z direction at $q_y = 0.0$ nm^{-1}. This component corresponds to diffuse scattering from the sample surface and the cap/nanodots and nanodots/substrate interfaces. The other is a pair of peaks at $q_y \simeq \pm0.2$ nm^{-1}, which correspond to the interparticle distance between the Ge nanodots. For 12.4 keV, the interparticle interference peaks extend in the q_z direction. On the other hand, the peaks bend inward at large q_z, particularly for the pattern at 22.5° with asymmetric distortion with respect to the q_z axis for 1.77 keV. Such distortion from what is expected by a straight section of the intensity in the reciprocal space might be observed when the effect of the curvature of the Ewald sphere is not negligible. The effect of the Ewald sphere is known to become apparent for GISAXS of gratings (Yan & Gibaud, 2007), where well defined alignment of artificial nanostructure is sensitive to the deviation from the

Bragg condition. Generally, such an effect is not appreciable for small-angle scattering of self-organized nanostructures where the spatial alignment, or the structure factor, is to some extent disordered. A SAXS pattern recorded with a two-dimensional detector usually represents an intensity map on the q_y–q_z plane in such cases. However, with a photon energy of 1.77 keV, *i.e.* with a seven times longer wavelength than conventional GISAXS, a Ewald sphere with one-seventh of the radius of that for hard X-rays is no longer approximated by a plane even in the small-angle region.

The size obtained by Guinier approximation from GISAXS patterns at 12.4 keV was 8.1 ± 0.3 nm regardless of the in-plane incidence angle, φ, and that obtained from the profiles at 1.77 keV was 8.2 nm. The sizes agreed with each other, suggesting that the form factors of the nanodots obtained for hard and soft X-rays at small q essentially agree.

Fig. 2(*a*) shows the change in a GISAXS pattern with in-plane rotation at 12.4 keV. The in-plane peak position, q_m, decreased with increasing in-plane rotation angle, φ, from [100] incidence of X-rays, and reached a minimum at [110] incidence. The average distance between Ge nanodots (L) is evaluated by

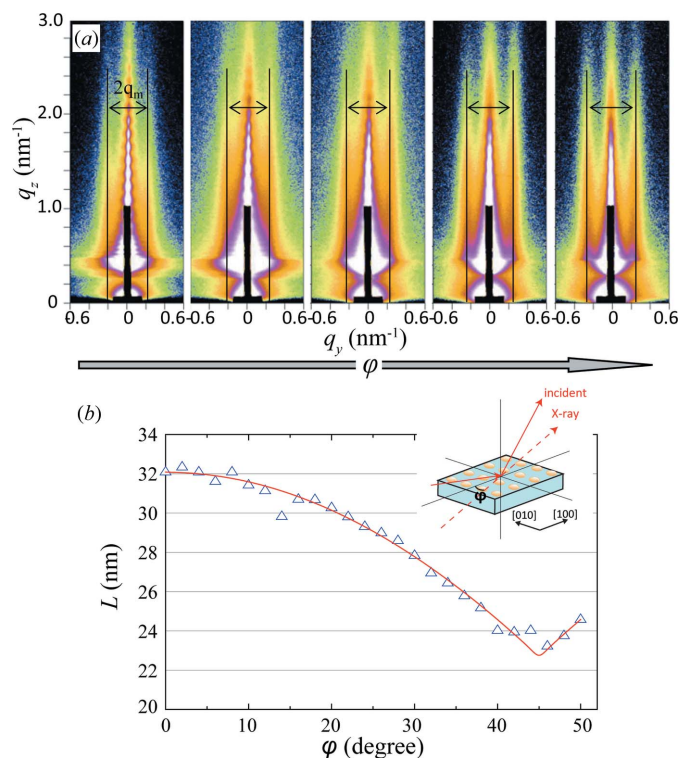$$L = 2\pi/q_m. \qquad (1)$$
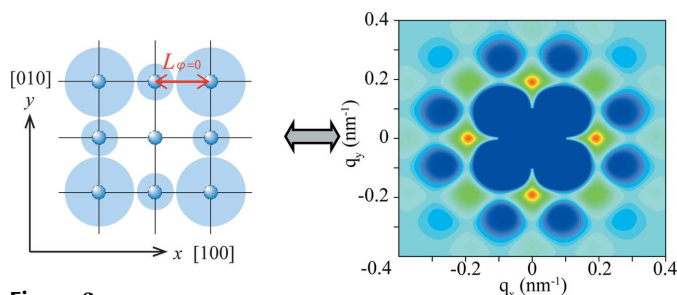
The distance was fit by the following equation,

$$L(\varphi) = \frac{L_0}{\cos[(\pi/4) - \varphi]}, \qquad \text{for} \quad 0 < \varphi < \pi/4. \qquad (2)$$
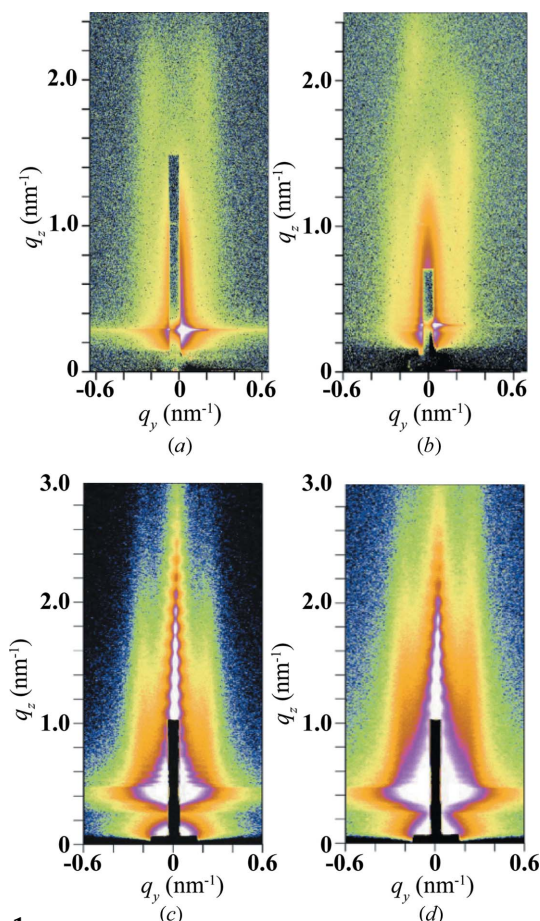
Figure 1
GISAXS patterns of Si-capped Ge nanodots in SX and HX regions. (*a*) $\varphi = 0°$ for SX, (*b*) $\varphi = 22.5°$ for SX, (*c*) $\varphi = 0°$ for HX, (*d*) $\varphi = 22.5°$ for HX.

Figure 2
(*a*) Change in the GISAXS pattern with in-plane rotation angle for hard X-rays. (*b*) Average distance between the nearest Ge nanodots (L) as a function of φ.
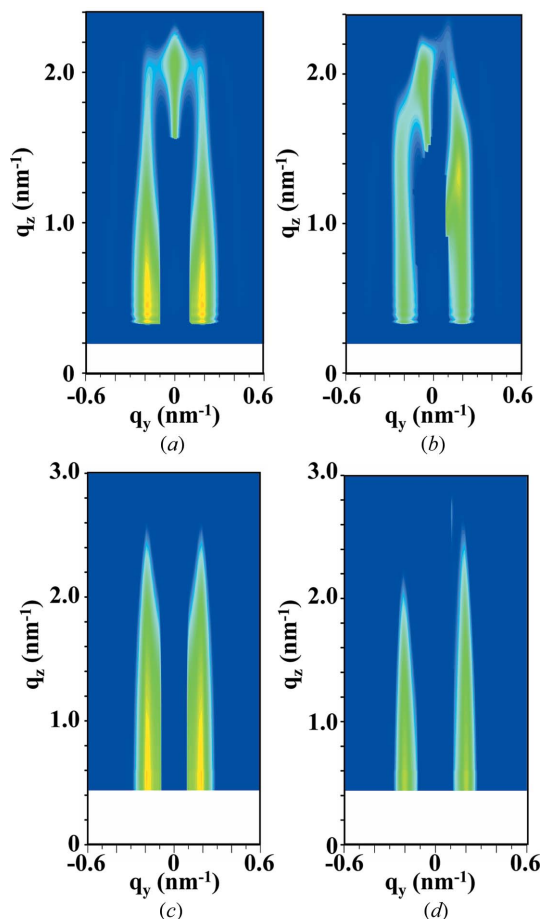
Figure 3
Schematic illustration of the spatial alignment of nanodots and the corresponding structure function used in the present model calculation; the grey area represents the probability distribution of the Ge nanodot location.

This implies that the spatial distribution of Ge nanodots on the substrate possesses fourfold symmetry as shown in Fig. 3. Such an effect can be explained in terms of elastic anisotropy of Si (Wortman & Evans, 1965; Brantley, 1973). In contrast, no appreciable anisotropy was observed for the gyration radius. Therefore, the present results suggest that the shape of the nanodots is isotropic in the in-plane direction but they are aligned preferentially along the main direction of Si $\langle 100 \rangle$, as sketched in Fig. 3. Considering that the elastic anisotropy is strong enough to result in anisotropic alignment, it is suggested that the anisotropy in the shape of the nanodots disappeared during growth of the Si cap layer (Schmidt & Eberl, 2000).

To demonstrate the GISAXS patterns in both energy regions and discuss the effects of Ewald sphere curvature, a model calculation was made with the DWBA (Sinha *et al.*, 1988). From a kinematical analysis of the GISAXS patterns as shown above, the shape of the Ge nanodots was modelled by flat domes of average height 2.2 nm and base radius 13.4 nm, as $F^2(q)$ (Ogawa *et al.*, 2005), whose shape was described by half an ellipsoid. The spatial alignment of the Ge nanodots was modelled as a structure factor, $S(q)$, aligning with fourfold symmetry and with Gaussian distance distribution using a paracrystal model with $\sigma = 0.2$, $L = 32.0$ nm, as schematically shown in Fig. 3 (Lazzari, 2002). The scattering intensity under the Born approximation is written as $I_B(q) = F^2(q)S(q)$. The layer parameters necessary for DWBA calculations were obtained from a least-squares fitting of the specular reflectivity. Roughnesses of 0.9 nm for the surface and 0.6 nm for the interface were obtained from the fitting (Okuda *et al.*, 2010).

Fig. 4 shows simulated GISAXS patterns for both soft and hard X-rays. It turned out that the dynamical effect added by the DWBA is apparent only near the Yoneda line, and does not affect the profile at higher q_z in the present case, in contrast to the block copolymer case (Busch *et al.*, 2007), where refracted beams generate additional Bragg spots or Debye rings from microphase-separated structures which alter the scattering profiles at moderately high q_z. Therefore, the characteristics of the present simulated patterns were understood by an intensity mapping of $I_B(q)$ on the Ewald sphere. In the HX region, the Ewald sphere is approximated by a plane in the small-angle region, and therefore scattering patterns

Figure 4
GISAXS intensity calculated for the model nanodot structure, with spatially Si-capped Ge nanodots self-organized on Si(001) using DWBA. (*a*) $\varphi = 0°$ for SX, (*b*) $\varphi = 22.5°$ for SX, (*c*) $\varphi = 0°$ for HX, (*d*) $\varphi = 22.5°$ for HX.

were similar to a cut of $I_B(q)$ on, for example, the q_y–q_z plane giving a symmetric GISAXS pattern. For hard X-rays, as shown in Figs. 4(*c*) and 4(*d*), the pair of straight interparticle interference peaks observed in the experiment was reproduced. The intensity for $q_y > 0$ is slightly stronger than that for $q_y < 0$, which agrees with Fig. 1(*d*), suggesting that a small effect can be detected even for hard X-rays under certain conditions. In contrast, the Ewald sphere cannot be approximated by a plane for soft X-rays, and the intensity distribution needs to be calculated on the Ewald sphere. Under such conditions the GISAXS pattern gave a symmetric distortion, showing typical narrowing of interparticle interference peaks at higher q_z when the in-plane structure was isotropic (Okuda *et al.*, 2009). Considering an anisotropic distribution of nanodots as discussed in the present work, the simulated intensity gave asymmetrically bent patterns with uneven maximum intensity, whose patterns agreed with the experiments. The only difference between the calculated patterns and the measurement is that a peak appears at $q_y = 0$ with higher q_z of about 2 nm^{-1} only in the calculation. A large curvature of the Ewald sphere results in the scattering vector coming closer to the neighbouring interparticle interference peaks at large q_z even in the small-angle region. This causes an apparent

increase in the scattering intensity around $q_z \simeq 2\,\text{nm}^{-1}$, and the increase in the interparticle interference peak at $q_z \simeq 2\,\text{nm}^{-1}$ is explained by this effect. The absence of a peak at $q_y = 0$ in the measured pattern, in contrast, implies that the domain size where Ge nanodots are aligned on a square lattice is larger in only one of the two in-plane [100] directions, and the peak of the structure function for 100, giving interparticle interference, is much stronger than that for 010, which gives a peak at $q_y = 0\,\text{nm}^{-1}$ and $q_z = 2\,\text{nm}^{-1}$. This model is reasonable considering atomic force microscopy and GISAXS observations showed that one-dimensional nanodot arrays were often observed for large nanodots (Schmidbauer *et al.*, 1999, 2002).

4. Conclusions

The effect of the curvature of the Ewald sphere on GISAXS patterns has been demonstrated by comparing the GISAXS intensities for Si-capped Ge nanodots self-organized on Si(001) for 1.77 keV (SX) and 12.4 keV (HX). Asymmetrically bent patterns and an intensity maximum at large q_z were observed for SX. From a DWBA model calculation, the characteristic patterns for SX were explained using the same $I_B(q)$ as that for HX. The differences in the scattering patterns between the profiles for the two X-ray regions were explained by the curvature of the Ewald sphere. It was concluded that GISAXS patterns with soft X-rays sometimes appear quite different from those with conventional hard X-rays, but they are quantitatively analyzed with the same structure model with different effects of the curvature of the Ewald sphere. The present results also imply that a direct approach for intensity mapping on the Ewald sphere will be an important tool for making full use of coherence imaging in the SX region.

References

Brantley, W. A. (1973). *J. Appl. Phys.* **44**, 534.
Busch, P., Posselt, D., Smilgies, D., Rauscher, M. & Papadakis, C. M. (2007). *Macromolecules*, **40**, 630–640.
Gibaud, A., Grosso, D., Smarsly, B., Baptiste, A., Bardeau, J. F., Babonneau, F., Doshi, D. A., Chen, Z., Brinker, C. J. & Sanchez, C. (2003). *J. Phys. Chem. B*, **107**, 6114–6118.
Kubler, L., Dentel, D., Bischoff, J. L., Ghica, C., Ulhaq-Bouillet, C. & Werckmann, J. (1998). *Appl. Phys. Lett.* **73**, 1053.
Lazzari, R. (2002). *J. Appl. Cryst.* **35**, 406–421.
Lee, B., Park, I., Yoon, J., Park, S., Kim, J., Kim, K., Chang, T. & Ree, M. (2005). *Macromolecules*, **38**, 4311–4323.
Levine, J. R., Cohen, J. B., Chung, Y. W. & Georgopoulos, P. (1989). *J. Appl. Cryst.* **22**, 528–532.
Li, J. H., Holý, V., Meduna, M., Moss, S. C., Norman, A. G., Mascarenhas, A. & Reno, J. L. (2002). *Phys. Rev. B*, **66**, 115312.
Metzger, T. H., Kegel, I., Paniago, R. & Peisl, J. (1999). *J. Phys. D*, **32**, A202–A207.
Müller-Buschbaum, P. (2013). *Polymer J.* **45**, 34–42.
Ogawa, H. *et al.* (2013). *Polymer J.* **45**, 109–116.
Ogawa, T., Niwa, H., Okuda, H. & Ochiai, S. (2005). *Mater. Sci. Forum*, **475–479**, 1097–1100.
Okuda, H., Kato, M., Kuno, K., Ochiai, S., Usami, N., Nakajima, K. & Sakata, O. (2010). *J. Phys. Condens. Matter*, **22**, 474003.
Okuda, H., Kato, M., Ochiai, S. & Kitajima, Y. (2009). *Appl. Phys. Express*, **2**, 126501.
Okuda, H., Ochiai, S., Ito, K. & Amemiya, Y. (2002). *Appl. Phys. Lett.* **81**, 2358–2360.
Okuda, H., Takeshita, K., Ochiai, S., Sakurai, S. & Kitajima, Y. (2011). *J. Appl. Cryst.* **44**, 380–384.
Petz, C. W. & Floro, J. A. (2011). *J. Appl. Phys.* **110**, 023508.
Rauscher, M., Paniago, R., Metzger, H., Kovats, Z., Domke, J. & Peisl, J. (1999). *J. Appl. Phys.* **86**, 6763–6769.
Renaud, G., Lazzari, R. & Leroy, F. (2009). *Surf. Sci. Rep.* **64**, 255–380.
Schmidbauer, M., Hanke, M. & Köhler, R. (2002). *Cryst. Res. Technol.* **37**, 3–34.
Schmidbauer, M., Wiebach, T., Raidt, H., Hanke, M., Köhler, R. & Wawra, H. (1999). *J. Phys. D*, **32**, A230–A233.
Schmidt, O. G. & Eberl, K. (2000). *Phys. Rev. B*, **61**, 13721–13729.
Sinha, S. K., Sirota, E. B., Garoff, S. & Stanley, H. B. (1988). *Phys. Rev. B*, **38**, 2297–2312.
Wortman, J. J. & Evans, R. A. (1965). *J. Appl. Phys.* **36**, 153.
Yan, M. & Gibaud, A. (2007). *J. Appl. Cryst.* **40**, 1050–1055.